

A molybdenum doped layer-spinel composite cathode material for sodium-ion battery

Sai Pranav Vanam^a, Prabeer Barpanda^{a,b,c,*}

^a Faraday Materials Laboratory (FaMaL), Materials Research Centre, Indian Institute of Science, Bangalore 560012, India

^b Helmholtz Institute Ulm (HIU), Electrochemical Energy Storage, Ulm 89081, Germany

^c Institute of Nanotechnology, Karlsruhe Institute of Technology (KIT), Karlsruhe 76021, Germany

ARTICLE INFO

Keywords:

Sodium-ion battery
P2-layer/spinel composite
P2-P2'' phase transition

ABSTRACT

Sodium-ion batteries are pursued as pragmatic alternative to the Li-ion battery technology having operational similarity along with natural resource abundance. P2-type manganese-rich layered oxides are widely explored exhibiting high capacity along with fast rate kinetics. To improve their electrochemical performance and reduce voltage decay upon cycling and to mitigate irreversible phase transitions, cation doping or hybrid composite integrations have been proposed. Here, we report a unique Mn-rich layer-spinel composite, $\text{Na}_{0.7}(\text{Li}_{1/18}\text{Mn}_{11/18}\text{Ni}_{3/18}\text{Fe}_{2/18}\text{O}_{2-x}\text{Na}_2\text{MoO}_4$, leading to a synergistic effect of layered P2 and spinel phases. This stable layer/spinel biphasic composite was stabilized through Mo doping and its electrochemical activity was studied at different voltage windows. When cycled between 1.5–4.5 V, this composite delivered a high specific capacity of 183 $\text{mAh}\cdot\text{g}^{-1}$ involving both cationic and anionic ($\text{O}^{2-}/\text{O}_2^{\cdot-}$) redox. The structural evolution during (dis)charge was studied by *ex-situ* X-ray diffraction and cyclic voltammetry. It is observed that mitigating P2-P2'' phase transition at higher voltage is crucial to improve the electrochemical performance, cycling stability and reduce the voltage hysteresis.

1. Introduction

Sodium-ion batteries (NIBs) are extensively investigated as possible alternatives for lithium-ion batteries (LIBs) particularly for large-scale stationary storage devices independent of gravimetric/volumetric energy density. Owing to the natural abundance, uniform geographic distribution and operational similarity, NIBs can indeed be harnessed as economic energy storage devices as demonstrated by their commercialization by M/s. CATL Inc., China (circa July 2021) [1]. In the pursuit to improve sodium storage performance, wide attention has been focused on the development of robust cathode materials with emphasis on layered oxides, polyanion compounds, and other electrode materials [2]. Here, layered sodium transition metal oxides, Na_xMeO_2 ($\text{Me} = 3d$ transition metals), have gained substantial attention due to their ease of synthesis, structural diversity and reversible Na^+ (de)insertion with high capacity. Due to the large ionic radius of Na^+ , layered Na_xMeO_2 polytypes vary according to oxygen cubic close packing (ccp) array forming P2 (ABBA stacking), P3 (ABCCA stacking), and O3 (ABCABC stacking) structures during chemical synthesis. As per Delmas notation, the symbols (O and P) denote octahedral and prismatic environment for sodium

sites and the numbers (2 or 3) indicate number of Me layers in the unit cell [3]. To date, P2 and O3 type oxide materials are reported as potential sodium-ion battery cathodes exhibiting high-rate kinetics and large capacity, respectively [4,5].

As compared to O3- type, the P2-type structure is more appealing because Na^+ ions can migrate across two face-shared trigonal prismatic sites in the Na layers, which facilitates higher rate capability. In this context, the Na-Ni-Mn-O system is a promising P2 type compound due to its high operating potential and energy density [6]. However, these compounds suffer from structural changes on over-extraction of Na^+ ions at higher voltages. These structural changes are induced by the gliding of MeO_2 slabs leading to O2-type structure with ABACAB oxygen packing, which results in irreversible structural collapse and capacity fading [6]. High electronegative cation substitutions like Li and Mg, which are electrochemically inactive, are generally used to suppress the unwanted phase transition [7]. Further, the electrochemical performance can be improved by doping active electrochemical cations (e.g. Co, Fe) [8,9]. Effective compositional manipulation can help to achieve larger capacities in Na-Ni-Mn-O quaternary cathode systems.

Another strategy to improve the electrochemical performance is by

* Corresponding author at: Faraday Materials Laboratory (FaMaL), Materials Research Centre, Indian Institute of Science, Bangalore 560012, India.
E-mail address: prabeer@iisc.ac.in (P. Barpanda).

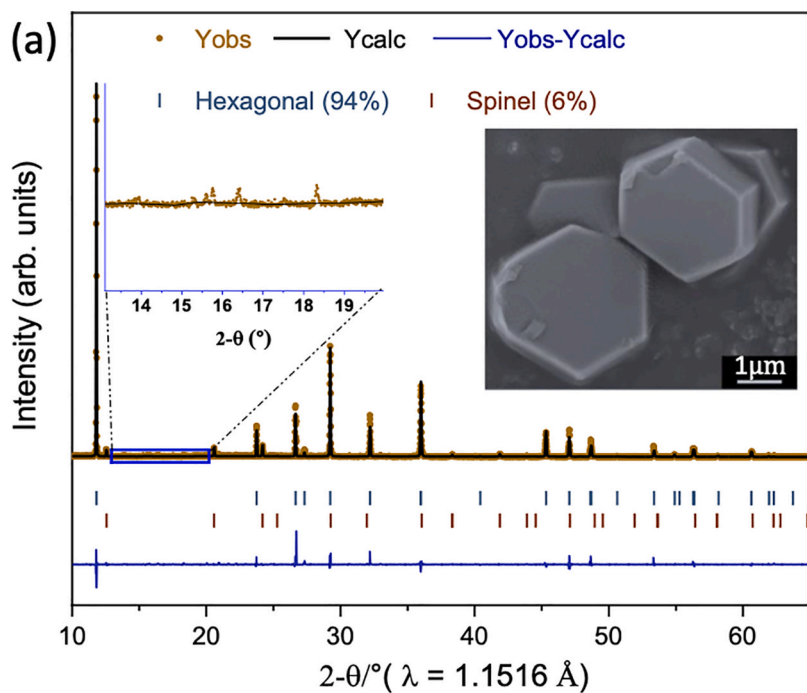
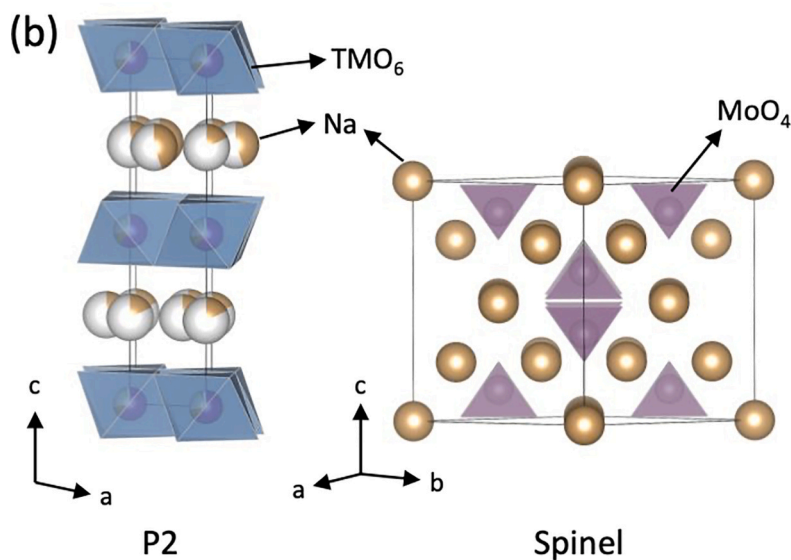


Fig. 1. Structural analysis of SMCO material. (a) Rietveld analysis of high-resolution synchrotron X-ray diffraction (SXR) pattern shows two phases: hexagonal layered P2 phase (94%) and spinel phase (6%). The observed data points (yellow), calculated pattern (black), their difference (blue) and two sets of Bragg peaks (blue and red vertical ticks) are shown. (inset) Representative SEM image of micrometric SMCO material. (b) Schematic illustration of crystal structures of layered (P2) and spinel phases.



employing composite cathodes. In biphasic composites, synergistic benefits of constituent phases can be exploited to optimize structural and electrochemical properties. For example, while the primary phase acts as active cathode, the secondary phase may impart structural stability during Na^+ (de)insertion and/or can suppress volume change during battery cycling [10]. Recently, bi- or multiphase hybrid composites were employed to yield high electrochemical performance and cycling stability [11,12]. The Li substituted O3 type layer-spinel intergrowth cathode material was shown to deliver capacity of 96 mAhg^{-1} after 100 cycles. Similar studies on integration of layer and spinel composites to boost electrochemical performance have been reported in LIBs [13]. Lately, spinel-integrated P2/P3-type layered composites have been examined as cathode material with fast rate kinetics. This synergistic led to cathodes with long life and high rates for SIBs [14,15]. In case of LIBs, Mo doped biphasic composites have been reported to deliver high-capacity retention vis-à-vis undoped cathode material [16]. Motivated by these studies, we adopted a strategy to synthesize P2 and spinel composite by doping redox

inactive Mo species. It is found that P2 and spinel target composite material $\text{Na}_{0.7}(\text{Li}_{1/18}\text{Mn}_{11/18}\text{Ni}_{3/18}\text{Fe}_{2/18}\chi_{1/18})\text{O}_2 - x\text{Na}_2\text{MoO}_4$ delivered a high specific capacity of 183 mAhg^{-1} stemming from both cationic ($\text{Mn}^{3+/4+}$, $\text{Ni}^{2+/3+/4+}$, $\text{Fe}^{3+/4+}$) and anionic ($\text{O}^{2-}/\text{O}_2^{\bullet-}$) redox activity. The material was investigated at different voltage windows to study the structural and electrochemical stability. With due optimization, this composite can act as a stable economic cathode for stationary sodium-ion batteries.

2. Experimental section

The target cathode composite material, $\text{Na}_{0.7}(\text{Li}_{1/18}\text{Mn}_{11/18}\text{Ni}_{3/18}\text{Fe}_{2/18}\chi_{1/18})\text{O}_2 - x\text{Na}_2\text{MoO}_4$ (referred as SMCO), was synthesized by co-precipitation method using a stoichiometric mixture of acetates of sodium, lithium, manganese, nickel along with iron nitrate and ammonium molybdate as precursors. These precursors were dissolved in a solution of water: ethanol (3:4) mixture. An aqueous solution mixed

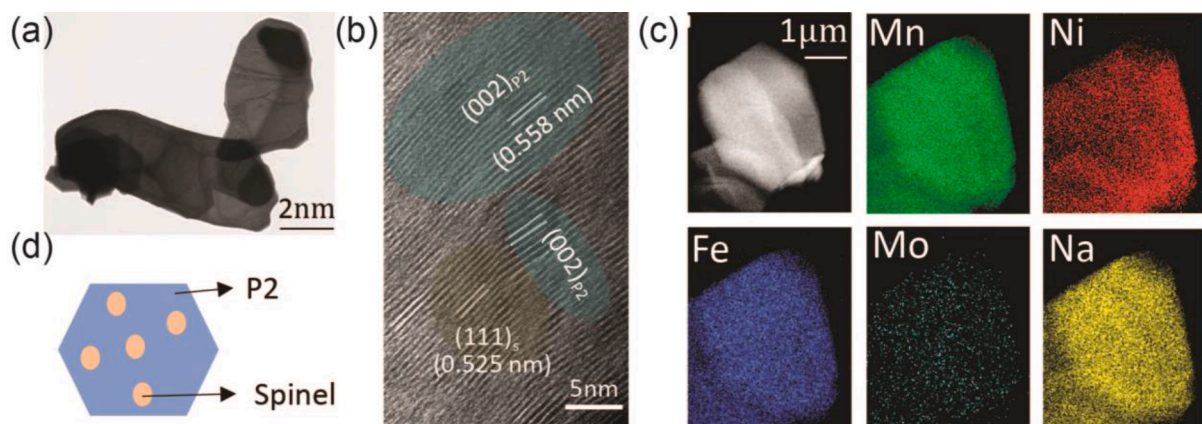


Fig. 2. Morphology and structure of composite SMCO. (a) Representative TEM image of SMCO reveals micrometric particle of size range 2–5 μm . (b) HR-TEM image of composite particle showing domains of layered P2 and spinel phases with d -spacing values of 0.558 nm [(002) plane of layered phase] and 0.525 nm [(111) plane of spinel phase] respectively. (c) EDS elemental maps of SMCO composite showing uniform distribution of all elements. (d) Pictorial presentation of composite cathode showing spinel phase embedded in P2 layered oxide phase.

with an excess amount of oxalic acid was added to the previous solution to form precipitates. The resulting co-precipitated solution was continuously stirred at 70 $^{\circ}\text{C}$ for 10 h before evaporating solvents at 110 $^{\circ}\text{C}$. The obtained powder was later calcined in a muffle furnace (heating rate = 5 $^{\circ}\text{C}/\text{min}$) at 900 $^{\circ}\text{C}$ for 5 h (in air) before cooling down to room temperature. The sample was immediately transferred inside an Ar-filled glove box to minimize any exposure to air/ moisture.

Powder X-ray diffraction (XRD) measurement was conducted on as-synthesized and *ex situ* sample using a PANalytical Empyrean X-ray diffractometer (PANalytical, Malvern, UK) equipped with a Cu $K\alpha$ source in the 2θ range of 10–70 $^{\circ}$ (step width = 0.026 $^{\circ}$). Following, synchrotron powder X-ray diffraction (SXR) was performed using X-ray radiation with wavelength 1.1516 \AA on Indian Beamline (BL-18B) at High Energy Accelerator Research Organization (KEK) Photon Factory (Tsukuba, Japan). The beamline energy was $E = 10.75$ keV, which was calibrated using LaB₆ standard sample. Rietveld analysis was performed using Fullprof software [17], and the structure was visualized using VESTA program [18]. Morphological analysis along with energy-dispersive X-ray spectroscopy (EDS) was conducted with a Carl Zeiss Ultra55 field-emission scanning electron microscope (FE-SEM, operating at 5 kV). Complementary transmission electron micrographs along with EDX maps were obtained using Titan Themis TEM unit (Thermo-FEI, operating at 300 kV). The specimen for HR-TEM measurement was prepared via dispersing powder in ethanol and drop-casting onto a copper grid, coated with a thin layer of amorphous carbon followed by drying under an infrared lamp. X-ray photoelectron spectra (XPS) of pristine and cycled electrodes were acquired with a Thermo scientific K-Alpha X-ray Photoelectron spectrometer using a monochromated Al target X-ray beam with $K\alpha$ radiation ($h\nu = 1486.6$ eV) (acceleration voltage = 12 kV, emission current = 6 mA). After Shirley background subtraction, the shift adjustments were conducted using a carbon signal as reference with a binding energy of 284.8 eV.

The electrochemical activity of $\text{Na}_{0.7}(\text{Li}_{1/18}\text{Mn}_{11/18}\text{Ni}_{3/18}\text{Fe}_{2/18}\chi_{1/18})\text{O}_2\text{-xNa}_2\text{MoO}_4$ sample was evaluated using coin-type cells (CR2032-type). Positive electrodes were made up of 80 wt% active materials, 10 wt% acetylene black, and 10 wt% poly(vinylidene fluoride) binder, mixed with N-Methyl-2-pyrrolidone (NMP) to adjust the viscosity of the slurry. This slurry was cast on Al foil using a doctor blade and was vacuum dried at 90 $^{\circ}\text{C}$ overnight. The composite cathode electrodes had a typical mass loading of 2.0 to 3.5 mg/cm^2 . For sodium half-cells, metallic Na foil was used as counter/reference electrode, and 1.0 M NaPF₆ dissolved in EC/DEC (1:1 by volume) (Kishida Chem. Co., Ltd.) was used as electrolyte soaked in porous Whatman glass fiber separator. Galvanostatic charge/discharge studies were performed using BTS-4000 (Neware, China) battery tester. Cyclic voltammetry and potentiostatic

intermittent titration technique (PITT) measurements were conducted using BCS 805/810 (Bio-Logic SAS, France) automatic battery cycler.

3. Results and discussion

3.1. Structural characterization of layer-spinel composite

Employing simple co-precipitation route, an intergrown layer (P2)-spinel composite, $\text{Na}_{0.7}(\text{Li}_{1/18}\text{Mn}_{11/18}\text{Ni}_{3/18}\text{Fe}_{2/18}\chi_{1/18})\text{O}_2\text{-xNa}_2\text{MoO}_4$ (χ indicates vacancy) (SMCO), was prepared. The crystal structure of as-synthesized SMCO compound was analysed with synchrotron powder X-ray diffraction (SXR) as shown in Fig. 1(a). A mixture of layered P2 (space group $P6_3/mmc$) and spinel (space group $Fd\bar{3}m$) phases could be indexed. The strongest diffraction peak at 11.85 $^{\circ}$ indicates (002) reflection of the P2 phase. The additional reflections (denoted by blue box) correspond to Li/Mn ordering in the TM layer [19]. The remaining diffraction peaks correspond to spinel Na_2MoO_4 byproduct compound, indicating the formation of layer + spinel (P2 + $Fd\bar{3}m$) composite material [20]. Rietveld analysis was conducted to further validate the phase fraction and lattice parameters in the SMCO composite, which was found to be composed of 94% of a dominant $P6_3/mmc$ (P2-hexagonal) phase with the lattice parameters of $a = b = 2.884(65)$ \AA and $c = 11.189(70)$ \AA and 6% of secondary spinel (Na_2MoO_4) phase with lattice parameter $a = 9.113(4)$ \AA . Details of the Rietveld analysis are summarized in Table S1. The schematic illustration of layer and spinel crystal structures is shown in Fig. 1(b). The formation of Na_2MoO_4 spinel phase reveals that Mo does not participate in forming P2 phase; rather it leads to a secondary spinel phase thus forming a layer-spinel composite. To validate the point, molybdenum-free $\text{Na}_{0.7}(\text{Li}_{1/18}\text{Mn}_{11/18}\text{Ni}_{3/18}\text{Fe}_{2/18}\chi_{1/18})\text{O}_2$ compound (SLMN) was synthesized, which showed no sign of spinel formation (ESI, Fig. S1a, Fig. S2) proving that even a small concentration of Mo (2.7 wt%) can trigger spinel formation. Considering the ionic radius and valence state of Mo^{+6} (0.59 \AA), molybdenum ions were expected to substitute in the Me slabs of sodium layered structures as observed in layered lithium oxides [21]. The absence of molybdenum in the structure could be due to the lower free energy formation of spinel Na_2MoO_4 phase. The interplanar spacing of (002) plane in both SMCO and SLMN materials was found to be 5.57 \AA (Fig. S1b). Hence, Mo doping has no effect on the d -spacing of the P2 layer structure i.e., all Mo species are consumed in spinel formation. During the calcination, the sodium concentration in the precursor was used in forming both phases (P2 + spinel). Considering the amount of Mo used in the synthesis, the back of the envelop calculations showed that 1/18 mol of sodium were used during spinel (Na_2MoO_4) formation, and the remaining ~ 0.64 mol were used in forming a layered P2 structure.

The final composition of the P2 layered oxide structure in the

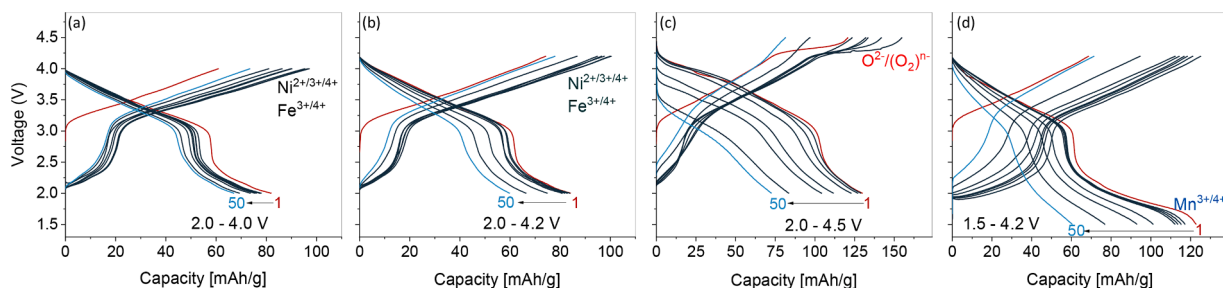


Fig. 3. Electrochemical performance of the SMCO composite electrodes in different voltage windows. The charge/discharge profiles of 1–50 cycles are shown at a current rate 0.1C for voltage windows of (a) 2.0–4.0 V, (b) 2.0–4.2 V, (c) 2.0–4.5 V, and (d) 1.5–4.2 V (vs. Na/Na⁺).

composite was deduced to be Na_{0.64}(Li_{1/18}Mn_{11/18}Ni_{3/18}Fe_{2/18}χ_{1/18})O₂. Previous studies have shown Ni stays in +2/+3 oxidation state in Na_{2/3}Ni_xMn_yO₂ compound by internal redox reaction [22,23]. Further, in Na_xFe_xMn_{1-x}O₂ (1.0 ≥ x ≥ 0.5), Fe is always found in +3 state [24]. Therefore, it is reasonable to assume that all Mn in the material exists in +4 oxidation state. To probe the oxidation states of constituent elements, XPS spectroscopy was conducted to capture the core peaks of SMCO powder (as shown in Fig. 4). Because of the spin-orbit coupling, 2p orbitals split into 2p_{3/2} and 2p_{1/2} components. The Ni 2p core peak showed two main components at 854.5 eV (Ni 2p_{3/2}) and 872.1 eV (Ni 2p_{1/2}), with satellite peaks at 860.7 and 878.8 eV respectively. The deconvolution of Ni 2p_{3/2} showed a mixture of Ni²⁺ and Ni³⁺ valence states to charge balance the compound. For element Fe, the 2p_{3/2} peaks at 711.5 eV and 716.7 eV can be assigned to Fe³⁺ and Fe⁴⁺ respectively [25]. While the Mn 2p core peak showed dominant peaks at 642.2 eV (Mn 2p_{3/2}) and 653.8 eV (Mn 2p_{1/2}) corresponding to a valence state of +4. This characterization could be beneficial for understanding the electrochemical properties of P2 layered-spinel composite as discussed in the later sections.

This layered-spinel composite was found to have hexagonal-shaped particles with micrometric morphology (3–5 μm) (Fig. 1a, inset). With or without Mo doping, similar morphology was observed (ESI, Fig. S3). Distinct P2 and spinel phases in the composite samples with the intergrowing interfaces were observed via high-resolution transmission electron microscopy (HRTEM) (Fig. 2a,b). The lattice fringes with the interplanar spacing of 5.58 Å and 5.25 Å can be ascribed to (002) plane of P2 phase and (111) plane of spinel phase, respectively. Energy-dispersive X-ray spectroscopy (EDS) elemental mapping confirmed

uniform distribution of all constituent elements (Na, Mn, Ni, Fe, Mo) in the composite sample (Fig. 2c). A pictorial representation of the composite material is rendered in Fig. 2d showing uniformly distributed spinel blocks in the P2 layered oxide matrix. These microscopic observations are in agreement with the SXRD results, confirming the formation of a layered P2/spinel composite structure.

3.2. Electrochemical study

The electrochemical performance of the single phase (SLMN) and composite structure (SMCO) was evaluated in sodium half cells (Fig. 3). The voltage ranges were selected considering the Mo redox nature in spinel Na₂MoO₄, which is inactive at higher voltages. The corresponding galvanostatic (dis)charge profiles (at a rate of 0.1 C) of SLMN and SMCO, cycled in the range of 2.0–4.0 V, are shown in Fig. S4 (ESI). Although, pristine SLMN delivered superior initial charge/discharge capacity (76/95 mAhg⁻¹) in comparison to SMCO compound (60/82 mAhg⁻¹, Fig. 3a), the composite cathode SMCO was found to exhibit superior capacity retention after 30 cycles [SMCO (85%) vis-à-vis SLMN (78%)]. Hence, our investigation was focused on the SMCO composite material. In both compounds, no voltage plateau corresponding to Na/vacancy ordering was observed, which indicates the constituent Na⁺ in interlayers are disorderly arranged [26].

By further raising the upper cutoff voltage to 4.2 and 4.5 V while restricting the lower cutoff voltage to 2.0 V, we studied the effect of cation/anion redox on the capacity (Fig. 3b, c). In case of 2.0 – 4.2 V range, there is no change in the voltage profile, but there is a slight (~2%) increase in the capacity. However, when the cell was cycled up to

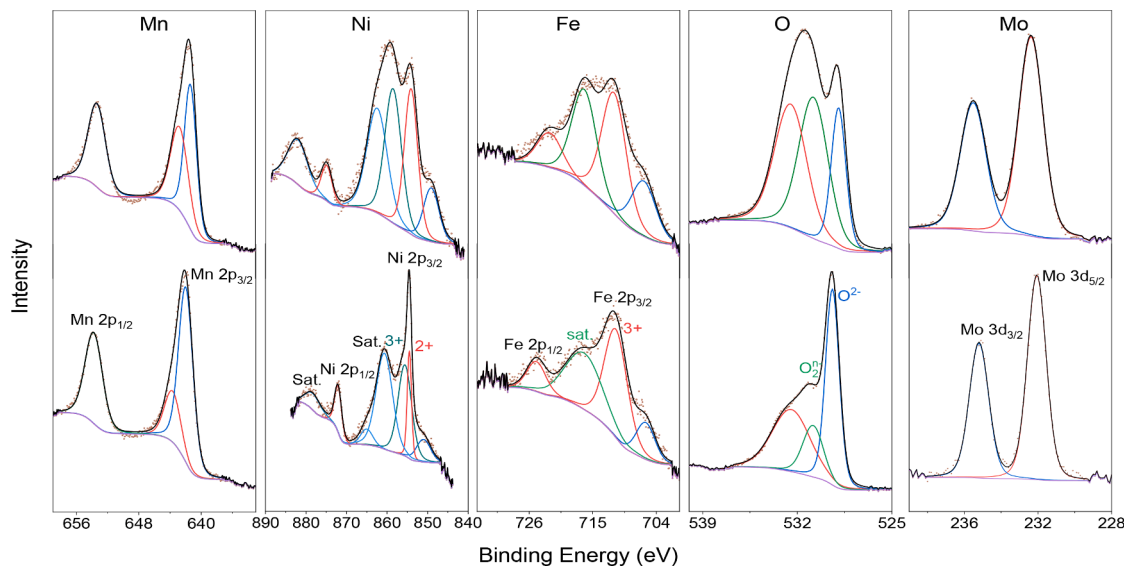


Fig. 4. Comparative XPS spectra of pristine and charged SMCO cathode showing the oxidation states of constituent species (Mn, Ni, Fe, O and Mo). (Bottom: pristine cathode, Top: charged cathode).

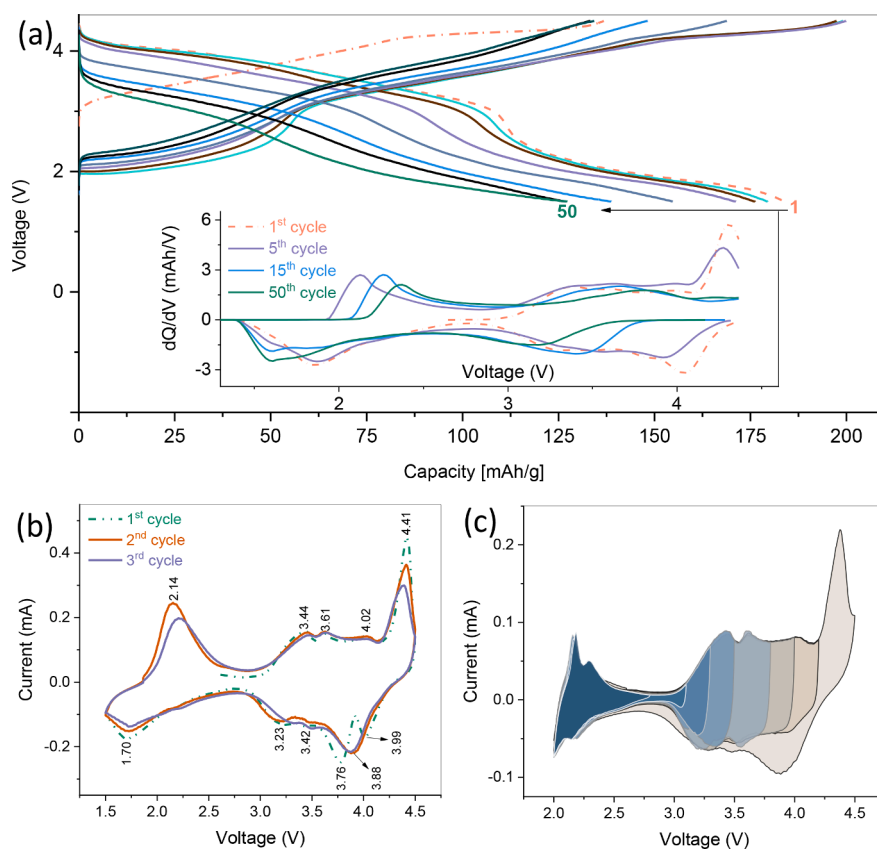


Fig. 5. Electrochemical performance SMCO composite cathode. (a) (Dis)charge voltage profiles showing 1- 50 cycles in the range 1.5–4.5 V (vs. Na/Na⁺). (Inset) Corresponding dQ/dV curves. (b) Cyclic voltammograms of three cycles (scan rate of 0.1 mV/s). (c) Voltammetric analysis with gradual increasing potential sweeps to probe the contribution of different redox centers.

4.5 V, during charge, a pseudo plateau at ~ 4.25 V was observed delivering an additional charge capacity of 47 mAhg^{-1} . However, during discharge, its corresponding plateau around 4.0 V has a considerable hysteresis. Nevertheless, upon charging till 4.5 V, a discharge capacity of 129 mAhg^{-1} was obtained Fig. 3b. On a practical note, this charge capacity is much higher than the estimated Ni^{2+/4+} and Fe^{3+/4+} redox activity (74 mAhg^{-1}), hinting at the involvement of other redox centers at higher potential. As the redox potential of Mn^{4+/5+} is expected to emerge at considerably very high potential and Li is a non-redox cation, this extra capacity at high voltage can be attributed to oxidation of lattice oxygen (i.e. anionic redox) [27,28].

It was noticed that after 50 cycles, approximately 81%, 71%, and 55% of capacity were retained for upper cut-off voltage of 4.0 V, 4.2 V, and 4.5 V, respectively. When all cationic redox centers were activated in the voltage range of 1.5 – 4.2 V, it led to severe capacity fading retaining $\sim 50\%$ at the end of 50 cycles (Fig. 3d). This capacity fading can be attributed to Mn reduction (Mn⁴⁺ to Mn³⁺) during discharge involving Jahn-Teller distortion of MnO₆ octahedra that can cause constraints and defects in the cathode. After 50 cycles (in the voltage window 2–4.5 V), the plateau ~ 4.2 V corresponding to anionic redox completely disappeared, which hints at irreversible O redox leading to O₂ release from the lattice. As anionic redox suffers from sluggish kinetic behavior in contrast to fast cation redox, we conducted the cycling at a low current rate of 0.05 C. The capacity fading and change in voltage profiles were found to be similar for both 0.05 C and 0.1C, which can be due to sluggish short-range atomic movements caused by repeated (O₂)ⁿ⁻ formation during (de)sodiation (ESI, Fig. S5).

Here, the pristine composite material contains redox active Ni, Fe, and Mn with oxidation states +2/+3, +3/+4, and +4, respectively. Upon charging till 4.2 V, the Ni and Fe act as active redox centers in delivering the capacity by oxidizing to +4 state. After 4.2 V, excess

capacity can solely be assigned to O²⁻/O⁻ redox corresponding to desodiation at higher voltages. The O redox may be triggered by Li-O-Na or χ -O-Na, or χ -O- χ configurations creating nonbonding oxygen 2p orbitals along the *c* axis. To investigate the oxidation states of elements, *ex situ* XPS spectra were collected at a fully charged state of 4.5 V (Fig. 4). As charging progresses, Ni³⁺ peaks shifted to higher binding energy as indicated by a peak at 858.8 eV that can be assigned to Ni⁴⁺ [29]. When charged to 4.5 V, the peak corresponding to Fe⁴⁺ increases indicating oxidation of Fe³⁺ to Fe⁴⁺. For the pristine cathode, the O peak at 529.3 eV refers to lattice O²⁻ anions. Upon charging, the peak of O₂⁻ merges suggesting the oxygen activity. This shows that O²⁻/O₂⁻ couple participate in delivering capacity at higher voltages. Throughout the charging process, Mn and Mo peaks showed no change in the binding energy indicating them as redox inactive. The O₂ release induces transition metal reduction during discharge, which may activate a cationic redox pair that was not exposed in the first charge [30]. In the following discharge (sodiation) upto 3 V, all the Ni and Fe species reduce back to +3 state. At voltage below 3 V, the capacity stems primarily due to Mn^{3+/4+} redox activity [31]. To validate this point, voltage window of 1.5–4.2 V was selected such that only cation redox centers can be activated in delivering capacity. The corresponding voltage profiles (Fig. 3d) widely differ from other profiles because of Mn^{3+/4+} redox activity at the lower voltage delivering an initial discharge capacity of 122 mAhg^{-1} . This net capacity is a combination of all cationic redox activity (Ni^{2+/3+/4+}, Fe^{3+/4+}, Mn^{3+/4+}).

To further probe the origin of capacity fading during charge/discharge (C/D), cyclic voltammetry (CV) was performed alongside C/D in the voltage window range of 1.5–4.5 V. Wide voltage window was chosen in order to cognize the nature of all redox peaks. The corresponding electrochemical C/D curves (Fig. 5a) reveals a combination of both cationic and anionic redox activity. CV plots showed four peaks in

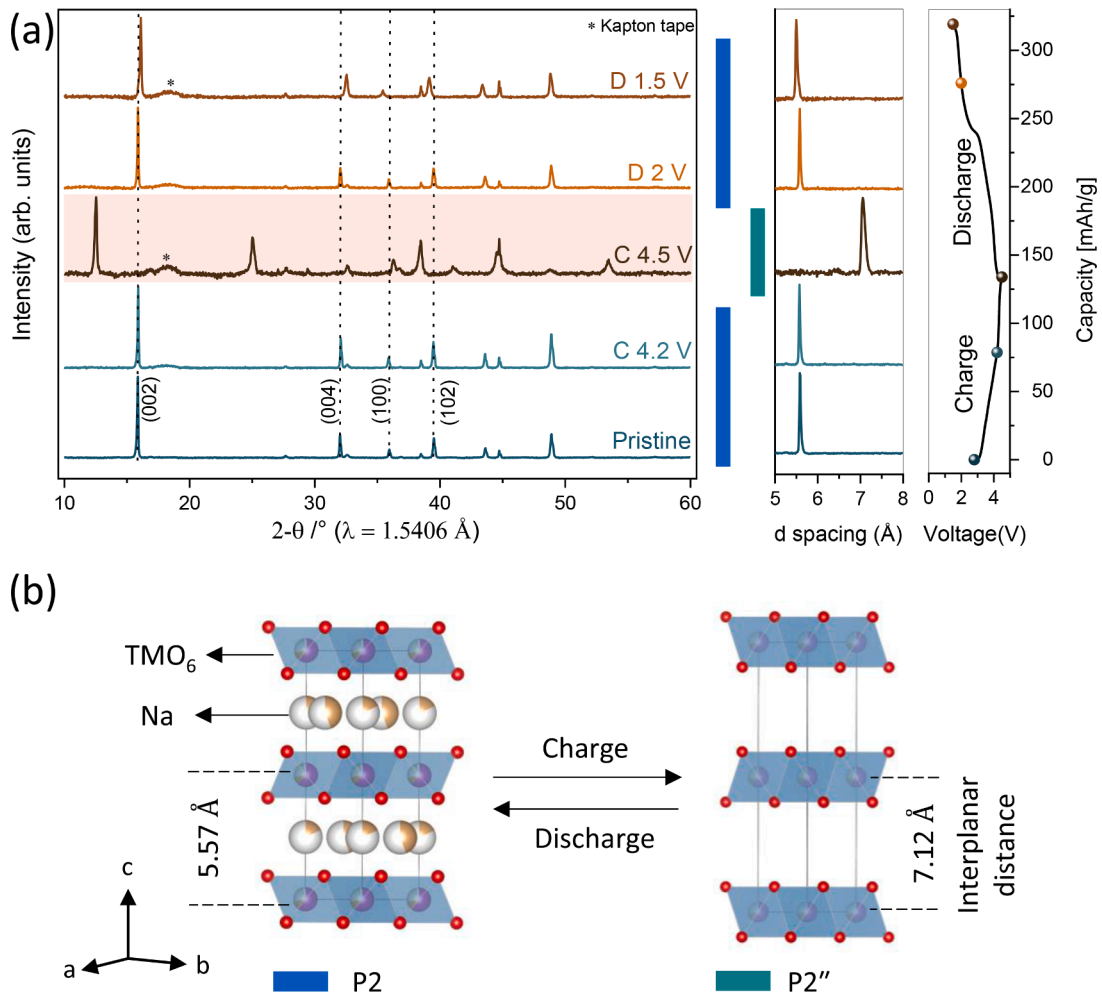


Fig. 6. (a) *Ex situ* XRD patterns at different voltages during the 1st charge and discharge processes. (b) Schematic illustration of the underlying P2 and P2' structural evolution.

the first anodic sweep related to $\text{Ni}^{2+/3+}$ (3.44 V), $\text{Ni}^{3+/4+}$ (3.61 V), $\text{Fe}^{3+/4+}$ (4.02 V), and O^{2-}/O_2 (4.41 V) redox steps [32–34]. On the following cathodic sweep, corresponding peaks for anionic and cationic redox steps were noticed (3.99 V, 3.76 V, 3.42 V, 3.23 V, and 1.70 V) along with an extra peak at a lower voltage (1.70 V) corresponding to $\text{Mn}^{4+/3+}$ redox appending additional storage capacity (Fig. 5b). In the subsequent cycles, the intense cathodic peak observed at 4.41 V broadened and the corresponding anodic peak shifted to lower voltages and merged into a broad peak at 3.88 V. The irreversible evolution of the redox peaks in the CV profiles suggests crystal structure relaxation/rearrangement, which could be related to various trend of cation migration at high voltage driving forces or linked to surface effects generated by different cation migration rates [35]. The differential voltage profiles (dQ/dV vs. V) show a comparable depiction (Fig. 5a, inset). The initial discharge capacity (183 mAhg^{-1}) results from the combination of redox activity of cations (Ni, Fe, Mn) and anion (O). This capacity gradually reduced with longer cycling. The intense peak at 4.2 V vanished after 15 cycles, referring to irreversible O_2 loss. The peaks corresponding to Ni and Fe also disappeared, and the Mn peaks shifted leading to inactive redox centers, which could be due to the transition metal migration associated with structural change [36]. To further investigate the structural changes and to couple the anionic and cationic peaks, a series of CVs were obtained by first applying a positive polarization with a scan rate of 0.1 mV.s^{-1} from OCV until 2.8 V followed by a negative polarization till 2 V. Afterwards, the polarization was gradually increased to 3.0, 3.3, 3.5, 3.8, 4.0, 4.2, and 4.5 V, with each step being

followed by negative polarization to 2 V (Fig. 5c). The lower voltage was restricted to 2 V as there are no distinguishable changes observed in the structural aspect as discussed later. The first anodic peak at 4.3 V was not significantly compensated upon negative polarization proving the irreversibility of anionic redox process. To understand the kinetic behavior and redox mechanism in the voltage range, potentiodynamic titration (PITT) study was conducted. The resulting profile revealed no change in the Cottrellian current behavior owing to single-phase topotactic reaction (ESI, Fig. S6). However, decay in the current response was observed for every potential step, suggesting the electrochemical process is limited by the diffusion of Na^+ ions [37]. Even the pseudo-plateau regime at 4.2 V did not reveal any bell-shaped curve suggesting it to be limited by Na^+ diffusion and not by the area of interface between the two phases [38].

To unveil the cause of capacity fading and the structural evolution during (de)sodiation, *ex situ* XRD patterns were acquired at different (dis) charged states of the first cycle as shown in Fig. 6a. As the sodium is deintercalated from the structure, the voltage curves display a linear increase in the potential upto 4.2 V. This smooth voltage profile suggests solid solution type redox mechanism in sync with CV and PITT studies. Similar behavior is observed in Li/Fe substituted transition metal layer of sodium layered oxide materials [24,39,40]. Upon desodiation till 4.2 V, no shift in the (hkl) reflections demonstrates no expansion or contraction due to repulsive interactions between oxygen along *c* axis and Na^+ ions in *ab* planes. At the end of charge (4.5 V) with near complete desodiation, a distinct new P2' phase was observed. This P2

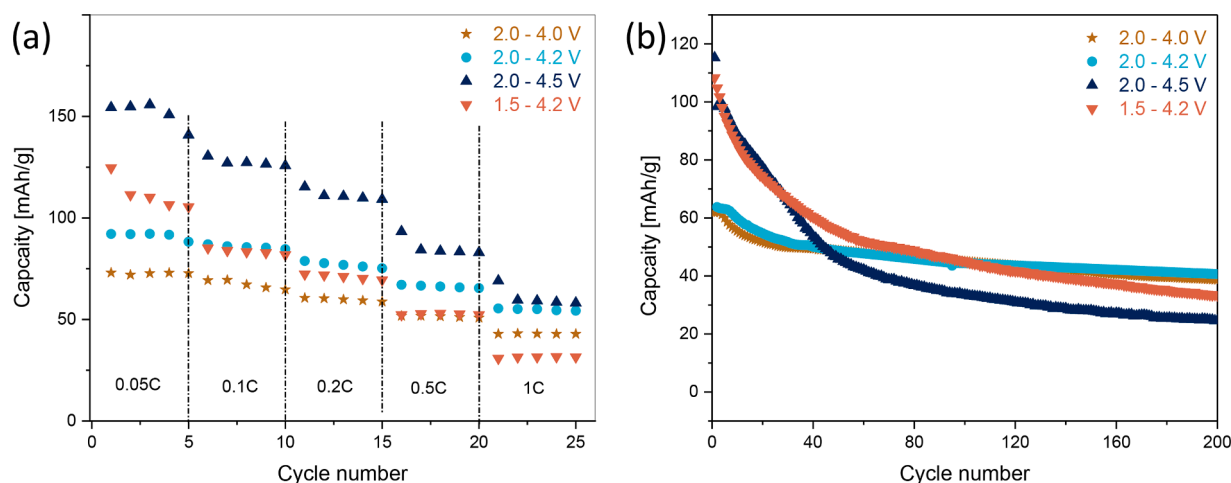


Fig. 7. (a) Discharge capacity of SMCO composite cathode when cycled at different rates (0.05C to 1C) and different voltage windows. (b) Cycling performance (at 1C) conducted at different voltage windows.

phase is denoted as P2'', where the peak asymmetric broadening suggested at the faulted layer structure. The P2'' phase has a larger interlayer distance (ca. 7.12 Å) in comparison to P2 phase (ca. 5.57 Å) (Figs. 6b, S7). Because of the anomalously large interplanar distance reported in sodium layered oxides, it is speculated that electrolyte solvent molecules and/or salts can be inserted between the slabs leading to a hydrated phase [41]. To prove the exact phase transitions, more precise *in-situ* synchrotron XRD study is warranted, which is beyond the scope of this work. On discharging (sodiation) till 2 V, the P2 phase was retained similar to the pristine cathode. On further discharging to lower voltage (1.5 V), (002) and (004) peaks shifted to higher angles indicating contractions along *c* axis because of reduced repulsive interactions between oxygen atoms in the interlayers, while (100) and (102) peaks shift to lower angles signifies expansion in *ab* plane due to enhanced Na⁺ ion repulsion.

The spinel Na₂MoO₄ phase remains inactive throughout the cycling. The complete structural transition is summarised in Fig. 6b illustrating sections of P2 and P2'' layered structure along (110) plane. The exact structure of ideal desodiated P2'' phase is not reported till date. At higher voltages, the formation of P2'' phase could result in a combination of oxygen loss and transition metal migration resulting in the capacity fading [36]. The increased polarization during discharge and gradual capacity fading validate this hypothesis. Overall, the P2-layer/spinel composite yield different electrochemical behavior when cycled at different voltage windows.

The cycling stability and rate capabilities at various voltage windows are shown in Fig. 7. The voltage range of 2.0 – 4.0 and 2.0 – 4.2 V offer stable capacity. As the voltage cutoff is lowered to 1.5 V, Jahn-Teller distortion of Mn³⁺ is observed, inducing structural instability (strain and distortions) in the layered material [42]. When cycled to higher voltage 4.5 V, the anionic redox accompanied by voltage hysteresis leads to capacity fading. The electrochemical performance of this P2-layer/spinel composite can be further improved by surface coating to stabilize the electrode/electrolyte interfaces and choice of suitable electrolyte composition to enable long-term operation of composite as sodium-ion cathode material.

4. Conclusions

In summary, a novel P2 layer-spinel composite, Na_{0.7}(Li_{1/18}Mn_{11/18}Ni_{3/18}Fe_{2/18}X_{1/18})O₂-xNa₂MoO₄, was successfully synthesized by Mo doping via facile co-precipitation method. Mo does not occupy transition metal position in P2 layer oxide, but instead form spinel Na₂MoO₄

secondary phase. This new P2 layered oxide-spinel composite, when employed as a cathode material in sodium half-cell, delivered a large discharge capacity of 183 mAh⁻¹ involving both cationic (Ni, Fe, Mn) activity at 2.5–4.0 V and anionic (O₂) redox activity at 4.2 V. We demonstrate the existence of O²⁻/O₂^{•-}/O₂ development as well as the oxygen release issue in SMCO, which occurs at higher voltages and results in significant capacity fading. Activating the Mn and O redox reaction at lower (2.5 V) and higher (4.2 V) voltage regions led to gradual capacity fading due to active Jahn-Teller distortion and O₂ evolution, respectively. Charging to very high voltage (ca. 4.5 V) triggered P2-P2'' phase transition, where the P2'' phase is quite similar to P2 phase (s.g. P6₃/mmc) with higher interplanar spacing involving transition metal migration and oxygen evolution leading to voltage hysteresis and capacity fading. By cycling in restricted voltage window, this P2-P2'' phase transition can be mitigated to yield stable electrochemical performance with reduced overpotential. A drastic improvement in the stability was seen in the voltage window of 2–4.0 and 2–4.2 V compared to others. This P2 layer-spinel composite can work as an economic cathode for secondary sodium-ion batteries.

CRediT authorship contribution statement

Sai Pranav Vanam: Conceptualization, Data curation, Formal analysis, Investigation, Methodology, Writing – original draft. **Prabeer Barpanda:** Conceptualization, Funding acquisition, Project administration, Supervision, Writing – review & editing.

Declaration of Competing Interest

The authors declare that they have no known competing financial interests.

Acknowledgments

The current work was financially supported by the Technology Mission Division (DST, Government of India) under the aegis of Materials for Energy Storage (MES-2018) program (DST/TMD/MES/2k18/00217). We thank the Department of Science and Technology for support to conduct synchrotron XRD study (at KEK-PF, Japan) and Dr. Gouranga Manna for his help in synchrotron experiment. P.B. is grateful to Alexander von Humboldt Foundation (Bonn, Germany) for a 2022 Humboldt fellowship for experienced researchers.

References

- [1] H.S. Hirsh, Y. Li, D.H.S. Tan, M. Zhang, E. Zhao, Y.S. Meng, Sodium-ion batteries paving the way for grid energy storage, *Adv. Energy Mater.* 10 (2020), 2001274, <https://doi.org/10.1002/AENM.202001274>.
- [2] D. Kundu, E. Talaie, V. Duffort, L.F. Nazar, The emerging chemistry of sodium ion batteries for electrochemical energy storage, *Angew. Chem. Int. Ed.* 54 (2015) 3431–3448, <https://doi.org/10.1002/ANIE.201410376>.
- [3] C. Delmas, C. Fouassier, P. Hagenmuller, Structural classification and properties of the layered oxides, *Phys. B+C.* 99 (1980) 81–85, [https://doi.org/10.1016/0378-4363\(80\)90214-4](https://doi.org/10.1016/0378-4363(80)90214-4).
- [4] S. Guo, P. Liu, H. Yu, Y. Zhu, M. Chen, M. Ishida, H. Zhou, A layered P2- and O3-type composite as a high-energy cathode for rechargeable sodium-ion batteries, *Angew. Chem. Int. Ed.* 54 (2015) 5894–5899, <https://doi.org/10.1002/anie.201411788>.
- [5] J. Zhang, W. Wang, W. Wang, S. Wang, B. Li, Comprehensive Review of P2-type $\text{Na}_{2/3}\text{Ni}_{1/3}\text{Mn}_{2/3}\text{O}_2$, a potential cathode for practical application of Na-ion batteries, *ACS Appl. Mater. Interfaces.* 11 (2019) 22051–22066, <https://doi.org/10.1021/acsami.9b03937>.
- [6] N. Yabuuchi, K. Kubota, M. Dahbi, S. Komaba, Research development on sodium-ion batteries, *Chem. Rev.* 114 (2014) 11636–11682, <https://doi.org/10.1021/cr500192f>.
- [7] Y. Sun, S. Guo, H. Zhou, Adverse effects of interlayer-gliding in layered transition-metal oxides on electrochemical sodium-ion storage, *Energy Environ. Sci.* 12 (2019) 825–840, <https://doi.org/10.1039/c8ee01006d>.
- [8] I. Hasa, S. Passerini, J. Hassoun, A rechargeable sodium-ion battery using a nanostructured Sb–C anode and P2-type layered $\text{Na}_{0.6}\text{Ni}_{0.22}\text{Fe}_{0.11}\text{Mn}_{0.66}\text{O}_2$ cathode, *RSC Adv.* 5 (2015) 48928–48934, <https://doi.org/10.1039/C5RA06336A>.
- [9] J. Choi, K.H. Kim, C.H. Jung, S.H. Hong, A P2-type $\text{Na}_{0.7}(\text{Ni}_{0.6}\text{Co}_{0.2}\text{Mn}_{0.2})\text{O}_2$ cathode with excellent cyclability and rate capability for sodium ion batteries, *Chem. Commun.* 55 (2019) 11575–11578, <https://doi.org/10.1039/c9cc05550a>.
- [10] K. Wang, Z.-G. Wu, G. Melinte, Z.-G. Yang, A. Sarkar, W. Hua, X. Mu, Z.-W. Yin, J.-T. Li, X.-D. Guo, B.-H. Zhong, C. Kübel, Preparation of intergrown P/O-type biphasic layered oxides as high-performance cathodes for sodium ion batteries, *J. Mater. Chem. A.* 9 (2021) 13151–13160, <https://doi.org/10.1039/D1TA00627D>.
- [11] G.K. Veerasubramani, Y. Subramanian, M.S. Park, B. Senthilkumar, A. Eftekhari, S. J. Kim, D.W. Kim, Enhanced sodium-ion storage capability of P2/O3 biphase by Li-ion substitution into P2-type $\text{Na}_{0.5}\text{Fe}_{0.5}\text{Mn}_{0.5}\text{O}_2$ layered cathode, *Electrochim. Acta* 296 (2019) 1027–1034, <https://doi.org/10.1016/j.electacta.2018.11.160>.
- [12] Q. Huang, J. Liu, S. Xu, P. Wang, D.G. Ivey, B. Huang, W. Wei, Roles of coherent interfaces on electrochemical performance of sodium layered oxide cathodes, *Chem. Mater.* 30 (2018) 4728–4737, <https://doi.org/10.1021/acs.chemmater.8b01556>.
- [13] D. Luo, G. Li, C. Fu, J. Zheng, J. Fan, Q. Li, L. Li, A new spinel-layered Li-rich microsphere as a high-rate cathode material for Li-ion batteries, *Adv. Energy Mater.* 4 (2014), 1400062, <https://doi.org/10.1002/aenm.201400062>.
- [14] P. Hou, J. Yin, X. Lu, J. Li, Y. Zhao, X. Xu, A stable layered P3/P2 and spinel intergrowth nanocomposite as a long-life and high-rate cathode for sodium-ion batteries, *Nanoscale* 10 (2018) 6671–6677, <https://doi.org/10.1039/C8NR00650D>.
- [15] J. Zheng, P. Yan, W.H. Kan, C. Wang, A. Manthiram, A spinel-integrated P2-type layered composite: high-rate cathode for sodium-ion batteries, *J. Electrochem. Soc.* 163 (2016) A584–A591, <https://doi.org/10.1149/2.0041605jes>.
- [16] W. Yan, X. Jia, S. Yang, Y. Huang, Y. Yang, G. Yuan, Synthesis of single crystal $\text{LiNi}_{0.92}\text{Co}_{0.06}\text{Mn}_{0.01}\text{Al}_{0.01}\text{O}_2$ cathode materials with superior electrochemical performance for lithium ion batteries, *J. Electrochem. Soc.* 167 (2020), 120514, <https://doi.org/10.1149/1945-7111/ABACEA>.
- [17] J. Rodríguez-Carvajal, Recent advances in magnetic structure determination by neutron powder diffraction, *Phys. B. Cond. Matt.* 192 (1993) 55–69, [https://doi.org/10.1016/0921-4526\(93\)90108-I](https://doi.org/10.1016/0921-4526(93)90108-I).
- [18] K. Momma, F. Izumi, VESTA 3 for three-dimensional visualization of crystal, volumetric and morphology data, *J. Appl. Crystallogr.* 44 (2011) 1272–1276, <https://doi.org/10.1107/S0021889811038970>.
- [19] L. Yang, X. Li, J. Liu, S. Xiong, X. Ma, P. Liu, J. Bai, W. Xu, Y. Tang, Y.-Y. Hu, M. Liu, H. Chen, Lithium-doping stabilized high-performance P2- $\text{Na}_{0.66}\text{Li}_{0.18}\text{Fe}_{0.12}\text{Mn}_{0.7}\text{O}_2$ cathode for sodium ion batteries, *J. Am. Chem. Soc.* 141 (2019) 6680–6689, <https://doi.org/10.1021/JACS.9B01855>.
- [20] J. Sun, J. Shen, T. Wang, Electrochemical study of $\text{Na}_{0.66}\text{Ni}_{0.33}\text{Mn}_{0.67-x}\text{Mo}_x\text{O}_2$ as cathode material for sodium-ion battery, *J. Alloy. Compd.* 709 (2017) 481–486, <https://doi.org/10.1016/J.JALLCOM.2017.02.200>.
- [21] T. Sattar, S.-H. Lee, B.-S. Jin, H.-S. Kim, Influence of Mo addition on the structural and electrochemical performance of Ni-rich cathode material for lithium-ion batteries, *Sci. Rep.* 10 (2020) 8562, <https://doi.org/10.1038/s41598-020-64546-8>.
- [22] J. Mao, X. Liu, J. Liu, H. Jiang, T. Zhang, G. Shao, G. Ai, W. Mao, Y. Feng, W. Yang, G. Liu, K. Dai, P2-type $\text{Na}_{2/3}\text{Ni}_{1/3}\text{Mn}_{2/3}\text{O}_2$ cathode material with excellent rate and cycling performance for sodium-ion batteries, *J. Electrochem. Soc.* 166 (2019) A3980–A3986, <https://doi.org/10.1149/2.0211916jes>.
- [23] J. Yoshida, E. Guerin, M. Arnauld, C. Constantin, B. Mortemard de Boisse, D. Carlier, M. Guignard, C. Delmas, New P2- $\text{Na}_{0.70}\text{Mn}_{0.60}\text{Ni}_{0.30}\text{Co}_{0.10}\text{O}_2$ layered oxide as electrode material for Na-ion batteries, *J. Electrochem. Soc.* 161 (2014) A1987–A1991, <https://doi.org/10.1149/2.0121414jes>.
- [24] J.S. Thorne, R.A. Dunlap, M.N. Obrovac, Structure and electrochemistry of $\text{Na}_x\text{Fe}_x\text{Mn}_{1-x}\text{O}_2$ ($1.0 \leq x \leq 0.5$) for Na-ion battery positive electrodes, *J. Electrochem. Soc.* 160 (2013) A361–A367, <https://doi.org/10.1149/2.058302JES/XML>.
- [25] R. Rajagopalan, B. Chen, Z. Zhang, X.L. Wu, Y. Du, Y. Huang, B. Li, Y. Zong, J. Wang, G.H. Nam, M. Sindoro, S.X. Dou, H.K. Liu, H. Zhang, Improved reversibility of $\text{Fe}^{3+}/\text{Fe}^{4+}$ redox couple in sodium super ion conductor type $\text{Na}_3\text{Fe}_2(\text{PO}_4)_3$ for sodium-ion batteries, *Adv. Mater.* 29 (2017), 1605694, <https://doi.org/10.1002/adma.201605694>.
- [26] P.-F. Wang, H.-R. Yao, X.-Y. Liu, Y.-X. Yin, J.-N. Zhang, Y. Wen, X. Yu, L. Gu, Y.-G. Guo, Na^+ /vacancy disordering promises high-rate Na-ion batteries, *Sci. Adv.* 4 (2018) eaar6018, <https://doi.org/10.1126/sciadv.aar6018>.
- [27] K. Du, J. Zhu, G. Hu, H. Gao, Y. Li, J.B. Goodenough, Exploring reversible oxidation of oxygen in a manganese oxide, *Energy Environ. Sci.* 9 (2016) 2575–2577, <https://doi.org/10.1039/C6EE01367H>.
- [28] B. Song, E. Hu, J. Liu, Y. Zhang, X.Q. Yang, J. Nanda, A. Huq, K. Page, A novel P3-type $\text{Na}_{2/3}\text{Mg}_{1/3}\text{Mn}_{2/3}\text{O}_2$ as high capacity sodium-ion cathode using reversible oxygen redox, *J. Mater. Chem. A.* 7 (2019) 1491–1498, <https://doi.org/10.1039/C8ta09422e>.
- [29] Y. Zhang, M. Wu, J. Ma, G. Wei, Y. Ling, R. Zhang, Y. Huang, Revisiting the $\text{Na}_{2/3}\text{Ni}_{1/3}\text{Mn}_{2/3}\text{O}_2$ cathode: oxygen redox chemistry and oxygen release suppression, *ACS Cent. Sci.* 6 (2020) 232–240, <https://doi.org/10.1021/acscentsci.9b01166>.
- [30] M. Ben Yahia, J. Vergnet, M. Saubanère, M.L. Doublet, Unified picture of anionic redox in Li/Na-ion batteries, *Nat. Mater.* 18 (2019) 496–502, <https://doi.org/10.1038/s41563-019-0318-3>.
- [31] X.H. Zhang, W.L. Pang, F. Wan, J.Z. Guo, H.Y. Lü, J.Y. Li, Y.M. Xing, J.P. Zhang, X. L. Wu, P2- $\text{Na}_{2/3}\text{Ni}_{1/3}\text{Mn}_{5/9}\text{Al}_{1/9}\text{O}_2$ microparticles as superior cathode material for sodium-ion batteries: enhanced properties and mechanism via graphene connection, *ACS Appl. Mater. Interfaces* 8 (2016) 20650–20659, <https://doi.org/10.1021/acsami.6b03944>.
- [32] H. Wang, B. Yang, X.Z. Liao, J. Xu, D. Yang, Y.S. He, Z.F. Ma, Electrochemical properties of P2- $\text{Na}_{2/3}[\text{Ni}_{1/3}\text{Mn}_{2/3}\text{O}_2]$ cathode material for sodium ion batteries when cycled in different voltage ranges, *Electrochim. Acta* 113 (2013) 200–204, <https://doi.org/10.1016/J.ELECTACTA.2013.09.098>.
- [33] S. Chu, S. Wei, Y. Chen, R. Cai, K. Liao, W. Zhou, Z. Shao, Optimal synthesis and new understanding of P2-type $\text{Na}_{2/3}\text{Mn}_{1/2}\text{Fe}_{1/4}\text{Co}_{1/4}\text{O}_2$ as an advanced cathode material in sodium-ion batteries with improved cycle stability, *Ceram. Int.* 44 (2018) 5184–5192, <https://doi.org/10.1016/j.ceramint.2017.12.124>.
- [34] Q. Shen, Y. Liu, X. Zhao, J. Jin, Y. Wang, S. Li, P. Li, X. Qu, L. Jiao, Transition-metal vacancy manufacturing and sodium-site doping enable a high-performance layered oxide cathode through cationic and anionic redox chemistry, *Adv. Funct. Mater.* 31 (2021), 2106923, <https://doi.org/10.1002/adfm.202106923>.
- [35] L. Yang, C. Chen, S. Xiong, C. Zheng, P. Liu, Y. Ma, W. Xu, Y. Tang, S.P. Ong, H. Chen, Multiprincipal component P2- $\text{Na}_{0.6}(\text{Ti}_{0.2}\text{Mn}_{0.2}\text{Co}_{0.2}\text{Ni}_{0.2}\text{Ru}_{0.2})\text{O}_2$ as a high-rate cathode for sodium-ion batteries, *JACS Au* 1 (2021) 98–107, <https://doi.org/10.1021/jacsau.0c00002>.
- [36] H. Hirsh, Y. Li, J.-H. Cheng, R. Shimizu, M. Zhang, E. Zhao, Y.S. Meng, The negative impact of transition metal migration on oxygen redox activity of layered cathode materials for Na-ion batteries, *J. Electrochem. Soc.* 168 (2021), 040539, <https://doi.org/10.1149/1945-7111/abf96e>.
- [37] J.B. Lee, J. Moon, O.B. Chae, J.G. Lee, J.H. Ryu, M. Cho, K. Cho, S.M. Oh, Unusual conversion-type lithiation in LiVO_3 electrode for lithium-ion batteries, *Chem. Mater.* 28 (2016) 5314–5320, <https://doi.org/10.1021/acs.chemmater.6b01053>.
- [38] E. Adamczyk, M. Gnanavel, V. Pralong, Redox activity of sodium vanadium oxides towards oxidation in Na ion batteries, *Materials (Basel)* 11 (2018) 1021, <https://doi.org/10.3390/ma11061021>.
- [39] J.S. Thorne, R.A. Dunlap, M.N. Obrovac, Investigation of P2- $\text{Na}_{2/3}\text{Mn}_{1/3}\text{Fe}_{1/3}\text{Co}_{1/3}\text{O}_2$ for Na-ion battery positive electrodes, *J. Electrochem. Soc.* 161 (2014) A2232, <https://doi.org/10.1149/2.0981414JES>.
- [40] L. Yang, L.Y. Kuo, J.M. López del Amo, P.K. Nayak, K.A. Mazzio, S. Maletti, D. Mikhailova, L. Giebeler, P. Kaghazchi, T. Rojo, P. Adelhelm, Structural aspects of P2-type $\text{Na}_{0.67}\text{Mn}_{0.6}\text{Ni}_{0.2}\text{Li}_{0.2}\text{O}_2$ (MNL) stabilization by lithium defects as a cathode material for sodium-ion batteries, *Adv. Funct. Mater.* 31 (2021), 2102939, <https://doi.org/10.1002/adfm.202102939>.
- [41] Z. Lu, J.R. Dahn, Intercalation of water in P2, T2 and O2 structure $\text{A}_z[\text{Co}_x\text{Ni}_{1/3-x}\text{Mn}_{2/3}\text{O}_2]$, *Chem. Mater.* 13 (2001) 1252–1257, <https://doi.org/10.1021/CM000721X>.
- [42] J. Zheng, P. Yan, W.H. Kan, C. Wang, A. Manthiram, A spinel-integrated P2-type layered composite: high-rate cathode for sodium-ion batteries, *J. Electrochem. Soc.* 163 (2016) A584–A591, <https://doi.org/10.1149/2.0041605jes>.